Species heterogeneity and synergy to boost photocatalytic hydrogen evolution

Jiankang Zhang,[a,#] Panzhe Qiao,[b,#] Hao Tan,[c] Lin Cui,[a] Zhan Zhou,[d] Dong Lin,[e] Yongxiao Tuo,[f,*] Yong Qin[a,g,*]

[a] Interdisciplinary Research Center of Biology & Catalysis, School of Life Sciences, Northwestern Polytechnical University, Xi'an 710072, P. R. China

[b] Shanghai Synchrotron Radiation Facility, Shanghai Advanced Research Institute, Chinese Academy of Science, Shanghai 201210, P. R. China

[c] School of Materials Science and Engineering, Peking University, Beijing 100871, P. R. China

[d] College of Chemistry and Chemical Engineering, Henan Key Laboratory of Function-Oriented Porous Materials, Luoyang Normal University, Luoyang 471934, P. R. China

[e] Max Planck-Cardiff Centre on the Fundamentals of Heterogeneous Catalysis FUNCAT, Cardiff Catalysis Institute, School of Chemistry, Cardiff University, Cardiff CF103AT, United Kingdom

[f] State Key Laboratory of Heavy Oil Processing, College of New Energy, China University of Petroleum (East China), Qingdao 266580, P. R. China

[g] State Key Laboratory of Coal Conversion, Institute of Coal Chemistry, Chinese Academy of Sciences, Taiyuan 030001, P. R. China

[*] Corresponding authors. E-mail addresses: yxtuo@upc.edu.cn; qinyong@nwpu.edu.cn

ABSTRACT: Integrating different reaction sites such as single atom (SA), nanocluster (NC) and oxygen vacancy (Ov) in a specific photocatalyst affords a new prospect to break through the limitation of SA catalysis. While the intrinsic influence mechanisms of cocatalyst size and Ov on photocatalytic performances and the synergy nature are still not well unraveled. Herein we report the synthesis and investigation of atomically dispersed Pt based photocatalysts surface-confined in Ov-containing porous TiO_2

nanoflowers by atomic layer deposition. The SA−NC coexisted $Pt_{SA+NC}@TiO_2$ photocatalysts exhibit the optimized hydrogen evolution activity (2260 h^{-1}), which is 3.6-fold higher than that of $Pt_{SA}@TiO_2$ counterparts. Moreover, the activity can be further remarkably enhanced to 3645 h^{-1} by engineering cocatalyst size and Ov concentration. We identify the ad-/desorption sites of reacting molecules and unravel the synergistic catalytic mechanisms of the active species by thorough characterizations and density functional theory calculations: Pt NC is responsible for the adsorption−dissociation of H_2O molecules preferentially adsorbed on Ti sites and meanwhile lowers the d-band center of Pt SA responsible for the desorption of H_2 molecule, and the adjacent Ov can well stabilize the cocatalysts and modify the electronic energy distribution of Pt NC achieving the optimized adsorption state toward the *OH intermediate. The present multiple sites engineering concept and mechanistic insights are expected to shed light on the rational design of atomically dispersed photocatalysts.

KEYWORDS: *Atomic layer deposition, Porous TiO_2, Pt single atoms and nanoclusters, Oxygen vacancy, Photocatalytic hydrogen evolution*

1. INTRODUCTION

Achieving efficient H_2 generation and realizing its application are the long-term pursuit of catalysis researchers,[1−3] and photocatalysis is an appealing and promising pathway for solar energy conversion into green H_2 from water splitting.[4−9] However, currently the photocatalytic performances are still limited by the poor light harvesting, easy charge-carrier recombination during migration and a high energy barrier for activating H_2O reactants.[8] These intrinsic problems can be addressed by controllably synthesizing photocatalysts with specific structure. In photocatalysis field, TiO_2 is still one of the most investigated benchmark photocatalysts due to its high chemical stability, environment-friendless and photocorrosion resistance, although it is limited to the narrow light absorbance range, low charge separation efficiency and sluggish proton reduction kinetics.[8−19] While these issues can be addressed by cocatalyst decoration

and/or defect engineering.

The cocatalyst decoration such as benchmark Pt on TiO_2 can not only improve the charge separation efficiency, but also lower the activation energy. Moreover, the cocatalyst sizes have a remarkable influence on the electron−hole separation and transfer, activation of reactant molecules and desorption of product molecules, which will finally generate a significant influence on the photocatalytic performances.[20−22] In photocatalytic hydrogen evolution (PHE) reactions, the atomically dispersed photocatalysts including SA-based photocatalysts generally exhibit much higher apparent and intrinsic PHE activity than the nanoparticle counterparts due to the ultral-high atom-utilization efficiency and unique physicochemical property.[23−28] However, SA is not beneficial for the activation of H_2O molecules,[29−31] which is generally considered to be the challenging and even rate-determining step in the water-involved reactions.[32,33] In this sense, integrating the reaction sites with different functions in a given photocatalyst affords a new prospect to break through the limitation of SA photocatalysts, which is especially true for multi-step reactions including the photocatalytic water splitting reaction.[34] Therefore, the heterogeneity of the active species is indispensable for the photocatalytic reaction. In fact, the ratios and roles of sub-/nanoclusters (NCs) are specially emphasized in the catalysis field in recent years, which not only possess high atom-utilization efficiency, but also present a certain metallic property favorable for the activation of H_2O molecules. The rational assembly of SAs and clusters responsible for different functions in a specific photocatalyst may lead to unexpected photocatalytic performances by utilizing their synergy.[30,31,35−37]

Besides, as a kind of intrinsic defect, oxygen vacancy (Ov) widely exists in reducible metal oxide materials such as TiO_2, MoO_3 and CeO_2, and Ov engineering has been demonstrated to be an effective and versatile strategy to modulate the catalytic performances in photocatalysis field because it can alter the bulk and sub-/surface physicochemical properties of the materials.[38−43] Resultantly, the photoresponsive range, charge transfer and separation, and subsequent surface reaction efficiency can be well modulated.[39−43] Moreover, the surface Ovs can also act as the reactive sites promoting the adsorption and activation of reactant molecules (e.g., H_2O molecules),

generating a synergistic effect with the adjacent cocatalysts by constructing the unique metal−Ov interfacial sites.[39–43] Therefore, synchronously engineering metal cocatalyst and Ov sites on reducible oxide semiconductor is a promising strategy to achieve the boosted photocatalytic performance, and a comprehensive and in-depth understanding toward the synergistic photocatalytic mechanism is also highly essential.

To this end, we designed and synthesized the Ov-containing porous anatase TiO_2 nanoflower confined Pt@TiO_2 photocatalysts with atomically dispersed SA and NC by atomic layer deposition (ALD), which can achieve the uniform deposition of metal on the 3D structure nanoflower supports via its self-limiting property.[44–46] The precise modulation of Ov and the cocatalyst size corresponding to the ratio of SA/NC were achieved by the following H_2 activation strategy. The constructed photocatalysts with multiple active sites including Pt SAs, NCs and adjacent Ovs exhibit the boosted PHE activity with a TOF of 3645 h^{-1} due to the remarkable SA−NC−Ov synergy. Multiple characterization techniques and density functional theory (DFT) calculations were employed to probe the adsorption−reaction sites of H_2O molecules, investigate the specific roles of Pt SA, NC and Ov, and unravel their synergistic photocatalytic mechanisms. Our present results strongly demonstrate the significance of reactive site heterogeneity in the photocatalytic reactions.

2. EXPERIMENTAL SECTION

2.1. Photocatalyst synthesis. Synthesis of TiO_2 nanoflower spheres: TiO_2 nanoflower spheres were synthesized by a slightly modified solvothermal method.[47] Specifically, 45 mL of N,N-dimethylformamide (DMF) and 135 mL of isopropyl alcohol (IPA) were mixed and then treated under ultrasonic conditions for 5 min. After that, 4.5 mL of tetrabutyl orthotitanate (TBT) was added to the above mixed solvent, which was then transferred to a Teflon-lined autoclave (250 mL) and heated for 20 h at 200 °C in an electric oven. After the reaction, the products were sequentially centrifuged, washed thoroughly with ethanol and dried at 60 °C overnight. Lastly, the collected white products were ground and then calcinated at 475 °C for 1.5 h in air obtaining the yellowish TiO_2 nanoflower sphere powders with hierarchical structures.

Synthesis of Pt@TiO_2 based photocatalysts by ALD: The ALD process was carried out in a homemade closed chamber-type ALD reactor. Briefly, the Pt ALD was performed to obtain the Pt@TiO_2 photocatalysts by sequential exposure of the above TiO_2 to $MeCpPtMe_3$ (Strem Chemicals, 99%) and O_3. Deposition temperature was set at 250 °C, and $MeCpPtMe_3$ contained in stainless steel bubbler was maintained at 60 °C. Ultrahigh purity nitrogen (99.999%) was used as the carrier and purge gas.

Hydrogen activation treatment: The activated Pt_{SA+NC}@TiO_2-xR (x represents reduction temperature) photocatalysts were obtained by hydrogen treatment (10%H_2/Ar, 45 min) under the temperatures of 175, 300 and 475 °C, respectively.

2.2. Photocatalyst characterizations. The SEM images were obtained by a scanning electron microscope (ZEISS Sigma 500, USA). Transmission electron microscopy (TEM), high-angle annular dark-field scanning TEM images and energy-dispersive X-ray spectroscopy mapping were collected on a FEI-Themis Z instrument operated at 300 kV. The XRD patterns were recorded by using a Philips X'Pert Pro Super X-ray diffractometer with Cu Kα radiation (λ = 1.540 Å). The X-ray photoelectron spectra were collected on an ESCALab-250 X-ray photoelectron spectrometer with an Al Kα source (1486.6 eV). H_2-TPR experiments were performed in a tubular quartz reactor (Micromeritics, AutoChem 2920), and the reduction was conducted in a 10% H_2/Ar atmosphere at a heating rate of 10 °C/min. The in situ diffuse reflectance infrared Fourier transform spectra of CO chemisorption (CO-DRIFTS) measurements were performed on a Bruker spectrometer. The X-ray absorption near edge structure and extended X-ray absorption fine structure spectra of the Pt L_3-edge were measured on the BL14W1 beamline of the Shanghai Synchrotron Radiation Facility. N_2 adsorption−desorption experiments were performed at 77 K (BSD-PS(M), Beishide Instrument Technology (Beijing) Co., Ltd.). The metal content of the catalysts was determined by inductively-coupled plasma optical emission spectroscopy (ICP−OES, Agilent 730). Diffuse reflectance ultraviolet−visible (UV−Vis) spectra of the samples were recorded in the region of 200−800 nm using a Thermo Scientific Evolution 220 spectrophotometer. After 40 mg of samples was weighed and then loaded into the quartz tube, the electron paramagnetic resonance (EPR) spectra were recorded

at room temperature (298 K) on a Bruker ESR5000 spectrometer using the following parameters: modulation amplitude of 0.2 mT, modulation frequency of 100 kHz, sweep time of 60 s and microwave power of 10 mW. To detect the Ti^{3+} signal, the low-temperature (77 K) EPR measurements were also performed on a Bruker A300-10/12 spectrometer with 1,1-Diphenyl-2-picrylhydrazyl (DPPH) as standard substance using the following parameters: modulation amplitude of 1 G, modulation frequency of 100 kHz, sweep time of 61 s and microwave power of 20 mW. The steady state photoluminescence (PL) spectra were recorded on a F98 fluorescence spectrophotometer (Shanghai Lengguang). The TA spectra were recorded on a commercial Ti/Sapphire regenerative amplifier laser system (Vitara, Astrella, Coherent Inc.) and an automated data acquisition transient absorption spectrometer (Helios Fire/EOS, Ultrafast Systems LLC). The samples (0.2 g mL^{-1} of water solution) were photoexcited under 350 nm pump laser and probed at the wavelength range from 400 to 640 nm. Global and target analyses were performed with the Glotaran software. Temperature-programmed desorption measurement of H_2O (H_2O-TPD) and H_2 (H_2-TPD) experiments were carried out on a Micromeritics AutoChem II 2920 chemisorption analyzer connected to a Hiden QIC-20 mass and TCD spectrometer, respectively.

2.3. Photocatalytic activity measurement. The evaluation of photocatalytic H_2 evolution activity were carried out in a top-irradiation reaction vessel connected to a closed gas circulation system under ultraviolet−visible light irradiation (350−780 nm, 300 W Xe lamp, 15 mA, 255 mW cm^{-2}, Beijing Perfectlight Technology Co., Ltd.). Typically, 50 mg of photocatalysts was dispersed in 100 mL of 20 vol% methanol−deionized water solution. Before irradiation, the reaction system, maintained at 5 °C by circulating cooling water, was vigorously stirred and thoroughly pumped. The amount of H_2 evolved was measured by using an on-line gas chromatograph equipped with a thermal conductivity detector (North Point Scientific, NP-GC-901, N_2 carrier).

The turnover frequency (TOF) was calculated according to the Eq. (1):

$$TOF = \frac{n_{H_2}}{n_{Pt} \times t} \qquad \text{Eq. (1)}$$

where n_{H2} is the mole number of H_2 generated, n_{Pt} is the total mole number of the Pt metal, and t is the reaction time.

The apparent quantum efficiency (AQE) of monochromatic light-derived H_2 production over the optimized $Pt_{SA+NC}@TiO_2$-475R photocatalyst was calculated from the Eq. (2), and the obtained wavelength-dependent AQE in 350 nm (4.78 mW cm^{-2}) was 9.4%.

$$AQE = \frac{2 \times \text{number of } H_2 \text{ molecules}}{\text{number of incident photons}} \times 100\% \qquad \text{Eq. (2)}$$

2.4. Photoelectrochemical measurement. The PEC characteristics of the samples were record using a standard three-electrode system (Ag/AgCl reference electrode and platinum foil counter electrode) on an electrochemical workstation (CHI760E instrument). The electrolyte was 0.5 M Na_2SO_4 solution. The working photoanodes were made by depositing sample slurry (1 mg sample, 0.7 mL deionized water, 0.3 mL isopropyl alcohol and 10 μL Nafion) on the fluorine doped tin oxid (FTO) glass. The measured vs. Ag/AgCl potential was converted to a reversible hydrogen electrode (RHE) scale using the Nernst equation: $ERHE = E_{Ag/AgCl} + 0.197 + 0.059\ pH$. A 300 W Xe lamp as the light source. Electrochemical impedance spectroscopy (EIS) was carried out in the frequency range of 0.05−105 Hz.

3. RESULTS AND DISCUSSION

3.1. Synthesis, Characterization and Activity Evaluation of the $Pt@TiO_2$ Photocatalysts.

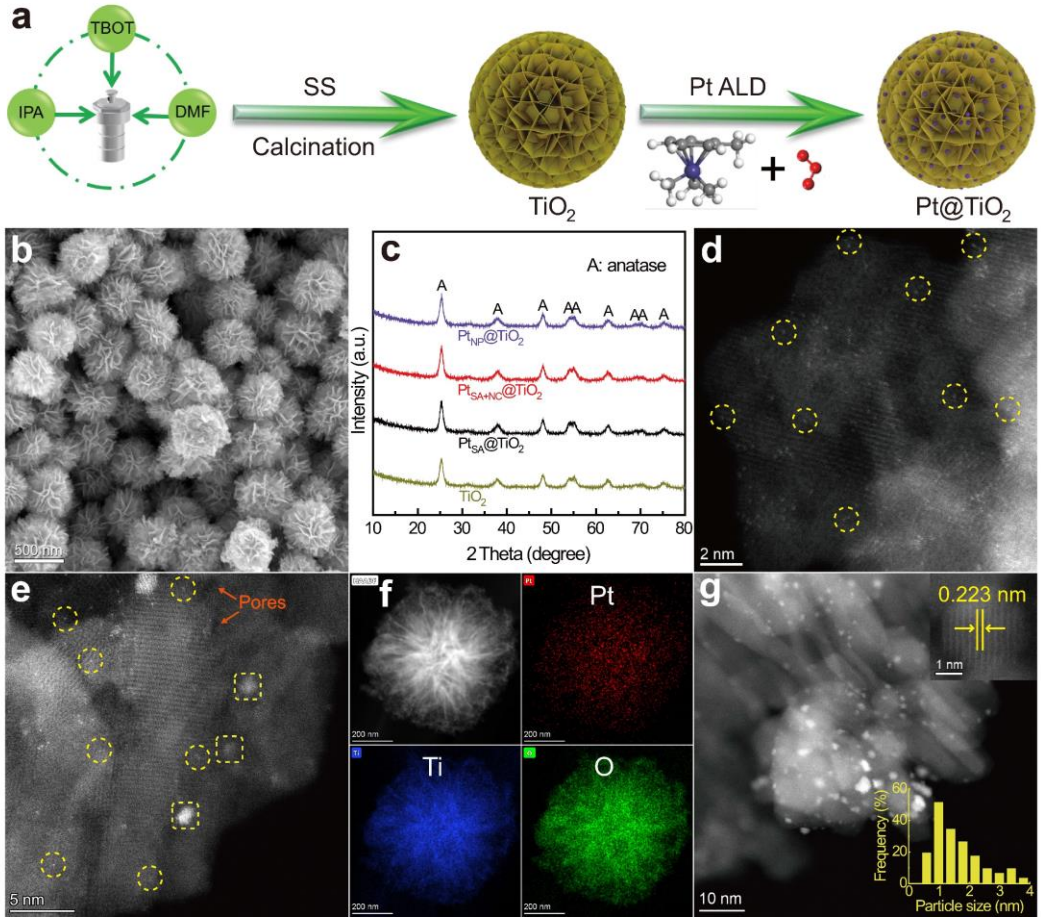

Figure 1. Synthesis and structure of the photocatalysts. (a) Synthetic process of the confined Pt@TiO_2 photocatalysts (TBOT, IPA and DMF represent tetrabutyl titanate, isopropanol and N,N-Dimethylformamide, respectively). (b) SEM image of the TiO_2 nanoflower spheres synthesized by solvothermal synthesis (SS). (c) XRD patterns of the four photocatalysts. (d) HAADF-STEM image of the Pt_{SA}@TiO_2 photocatalysts. (e) HAADF-STEM and (f) the corresponding elemental mapping images of the Pt_{SA+NC}@TiO_2 photocatalysts. (g) HAADF-STEM, HRTEM images (inset) and the corresponding histogram of particle size distribution (inset) of the Pt_{NP}@TiO_2 photocatalysts.

The porous anatase TiO_2 nanoflower spheres with a wide open-mouth structure and rich Ov (yellowish powder) were successfully synthesized by a slightly modified solvothermal method (Figures 1a−c),[47] which were used as supports to load Pt cocatalysts. The layered structures and mesoporous channels of TiO_2 hierarchical spheres can not only make the reactant molecules highly accessible to the surface-confined Pt cocatalysts, but also inhibit the sintering of Pt cocatalysts by the unique surface confinement effect. Then the high-dispersion Pt cocatalysts were deposited and confined in the surficial pores of TiO_2 nanospheres by Pt ALD, obtaining the surface-confined Pt@TiO_2 photocatalysts with different cocatalyst sizes, which can be achieved

by simply adjusting the ALD cycle numbers. Aberration-corrected high-angle annular dark-field scanning transmission electron microscopy (HAADF-STEM) was adopted to characterize the microstructures of the photocatalysts (Figures 1d−g and S1−3). Figures 1d and S1 are the HAADF-STEM images of the $Pt_{SA}@TiO_2$ photocatalysts (0.012 wt%), and the Pt SAs labeled with yellow circles are highly dispersed on the TiO_2 support. With the further increase of Pt content to 0.034 wt% (Figures 1e and S2), the SA−NC coexisted $Pt_{SA+NC}@TiO_2$ photocatalysts were achieved, whose main species are still SAs coexisting with certain amounts of NCs (labelled with yellow squares). Careful examinations of the NCs indicate that they are composed of randomly assembled Pt atoms (nearly atomic clusters), still exhibiting atomically dispersed features. The photocatalysts were further characterized by energy-dispersive X-ray spectroscopy (EDS) mapping (Figure 1f), which again confirms the uniform distribution of the Pt on TiO_2. Note that the black dots are the formed pores (Figures 1e and S1b), demonstrating the porous structures of the synthesized TiO_2. With the further increase of Pt contents to 1.78 wt%, Pt nanoparticles (NPs) with a mean particle size of approximately 1.61 nm can be observed (Figures 1g and S3). The measured lattice spacing of the well-crystallized nanoparticle is *ca.* 0.223 nm (inset in Figure 1g), which corresponds well to the Pt(111) plane.[32] Besides, the lattice spacing of *ca.* 0.35 nm (inset in Figure S1b) is ascribed to the anatase TiO_2(101) plane,[48] consisting well with the above XRD results (Figure 1c).

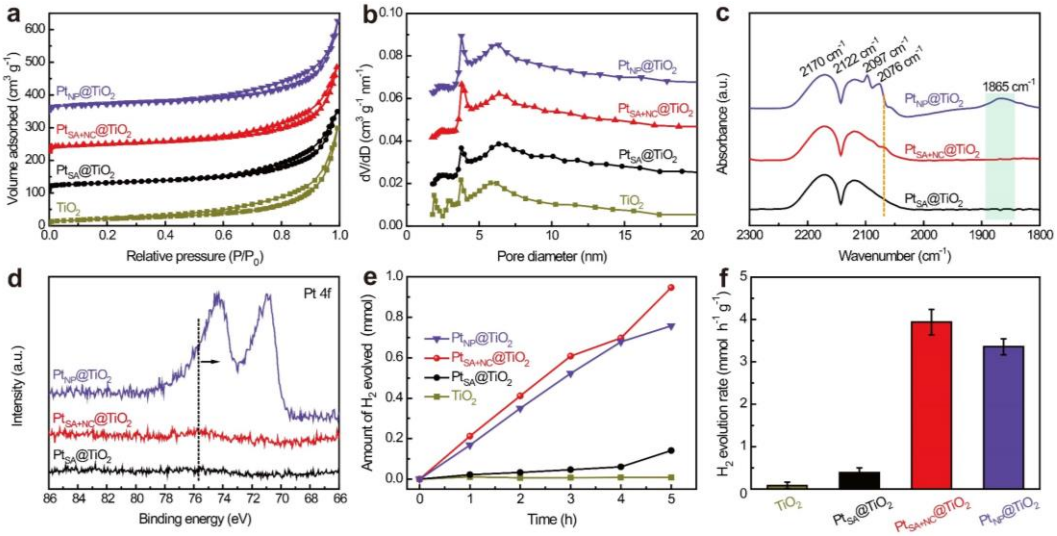

Figure 2. Physicochemical properties and activity evaluation of the photocatalysts. (a) N_2

adsorption−desorption isotherms and (b) the corresponding pore size distribution curves of the four photocatalysts. (c) CO-DRFITS spectra of the three photocatalysts. (d) XPS Pt 4f spectra of the three photocatalysts. (e) The continuous profiles of photocatalytic H_2 evolution (20 vol% methanol−aqueous) and (f) the corresponding H_2 evolution rates over the photocatalysts (50 mg) under ultraviolet−visible (UV−Vis) light irradiation.

The physicochemical properties of the photocatalysts were investigated by multiple characterizations. Figures 2a and 2b show the texture properties of the photocatalysts. The adsorption−desorption isotherms present characterizations of both type II and III isotherms, indicating that the photocatalysts possess the hierarchical pore structures. There is a slight decrease in view of the total pore volume for the decorated photocatalysts due to the deposition of Pt cocatalysts into the pores of TiO_2 (Table S1), which can be further verified by the disappearance of pores with the smaller pore diameter (*ca.* 1.9 nm). The diffuse reflectance infrared Fourier transform spectroscopy of CO adsorption (CO-DRIFTS) on the photocatalysts were further performed to reveal the geometric structures of Pt cocatalysts by analyzing the CO adsorption behaviors on the Pt cocatalysts (Figure 2c). The peaks at around 2170 and 2122 cm^{-1} are identified as the gas-phase CO molecule vibrations.[49] No observable peak is detected except the two CO peaks from the spectrum of $Pt_{SA}@TiO_2$ photocatalysts. There exists a weak peak at around 2067 cm^{-1} in the spectrum of $Pt_{SA+NC}@TiO_2$ photocatalysts, and the peak could be assigned to CO molecules adsorbed at edge and/or corner sites of low-coordination Pt clusters,[50,51] which present a red shift in $Pt_{NP}@TiO_2$ photocatalysts. Moreover, the peaks at around 2097, 2076 and 1865 cm^{-1}, only detected in the spectrum of $Pt_{NP}@TiO_2$ photocatalysts, can be ascribed to the linear and bridge bonding of CO molecules on large nanoclusters and/or metallic nanoparticles with well-coordinated Pt sites, respectively.[51] Especially, the bridge-bonded peak strongly demonstrates the existence of nanoparticles in the $Pt_{NP}@TiO_2$ photocatalysts, consisting well with the above HAADF-STEM results. To determine the electronic states of Pt cocatalysts with different size, X-ray photoelectron spectroscopy (XPS) was performed. From the survey spectra of the photocatalysts (Figure S4), Pt, Ti, O and trace N were all detected, again indicating the sucessful decoration of Pt on TiO_2. Moreover, the peak intensity increases monotonely with the increased Pt contents, and the Pt 4f binding energy

gradually shifts to the lower position with increased Pt size (Figure 2d) due to the metal size effects, which would further influence the photocatalytic performances.

The photocatalytic hydrogen evolution performance of the TiO_2, $Pt_{SA}@TiO_2$, $Pt_{SA+NC}@TiO_2$ and $Pt_{NP}@TiO_2$ photocatalysts were measured in the methanol−aqueous solution. With the bare TiO_2 as photocatalysts, only trance amount of H_2 is generated (0.08 mmol h^{-1} g^{-1}, Figures 2e, 2f and Table S1). After decoration of Pt SAs on the TiO_2, the PHE rate is approximately increased by 4 times compared with that of the bare TiO_2. Impressively, the PHE rate increases to optimized 3.94 mmol h^{-1} g^{-1} with $Pt_{SA+NC}@TiO_2$ as photocatalysts, which is approximately 10-fold higher than that of $Pt_{SA}@TiO_2$ counterparts. While the $Pt_{NP}@TiO_2$ photocatalysts with larger particle size and higher content present the decreased PHE activity, indicating that high-loading Pt cocatalyst with NP size contributes little to activity enhancement and even results in the decreased activity.[31,52] The corresponding turnover frequency (TOF) value of $Pt_{SA+NC}@TiO_2$ is *ca.* 2260 h^{-1} (Table S1), which is 3.6 and 61-fold higher than that of $Pt_{SA}@TiO_2$ and $Pt_{NP}@TiO_2$ counterparts, respectively. These results indicate that the remarkable synergy between the SA and NC contributes to the boosted PHE activity.

3.2. Activation Treatment and Structure Characterization.

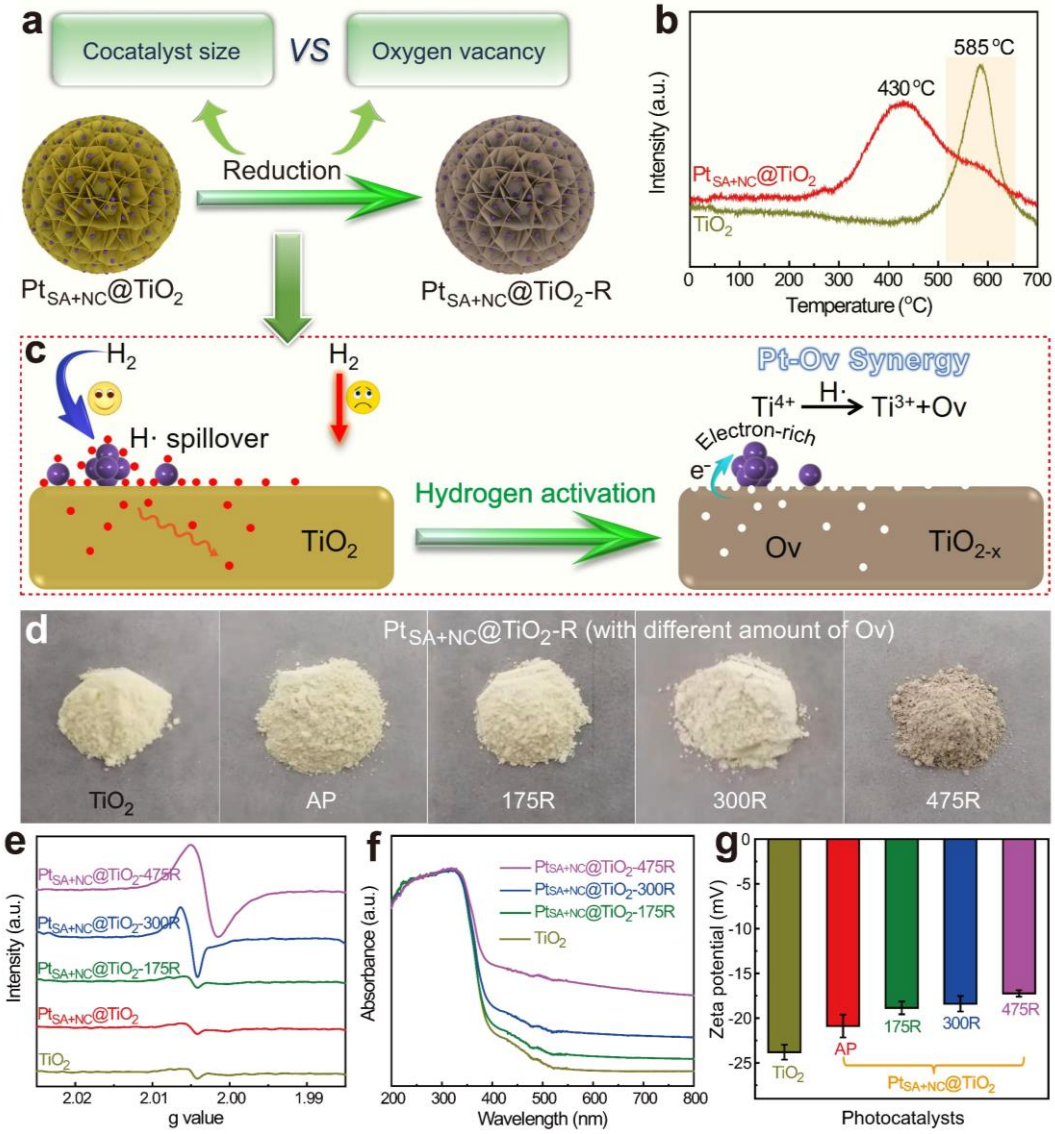

Figure 3. Structure modulation and characterization. (a) The modulation of cocatalyst size versus Ov concentrations by H_2 activation treatment. (b) H_2-TPR profiles of bare TiO_2 and $Pt_{SA+NC}@TiO_2$ photocatalysts. (c) Schematics of active spillover H· effect. (d) The color comparison of the photocatalysts (AP represents as-prepared). (e) EPR spectra obtained at 298 K, (f) UV−Vis spectra and (g) the zeta potential of the photocatalysts.

To investigate the cocatalyst size and Ov concentration on the influence of photocatalytic activity, the above optimized $Pt_{SA+NC}@TiO_2$ photocatalysts were further reduced by H_2 under different temperatures (Figure 3a). Figure 3b is the H_2-temperature programmed reduction (H_2-TPR) profiles of bare TiO_2 and $Pt_{SA+NC}@TiO_2$ photocatalysts. For the H_2-TPR profile of bare TiO_2, there is a narrow hydrogen consumption peak at high temperature (around 585 °C), which should be assigned to the partial reduction of TiO_2 ($Ti^{4+} \longrightarrow Ti^{3+}$ + Ov).[53] While the high-temperature

reduction peak becomes quite weak, and a new wide hydrogen consumption peak at low temperature (around 430 ºC) can be observed from the profile of the $Pt_{SA+NC}@TiO_2$ photocatalysts, indicating that TiO_2 can be partially reduced at a much lower temperature due to the strong hydrogen spillover effect from Pt to TiO_2 (Figure 3c). This can be verified from the color changes of the photocatalysts before and after reduction/activation treatment: the color of as-prepared $Pt_{SA+NC}@TiO_2$ photocatalysts changes from yellowish to light grey because a small amounts of Ti^{4+} are reduced to Ti^{3+} accompanied with the formation of new Ovs (Figure S5) under the treatment condition of 300 ºC, corresponding to the initial reduction temperature of TiO_2 (Figure 3b). Note that the color of $Pt_{SA+NC}@TiO_2$-475R photocatalysts becomes oxford grey, while the color change is relatively not obvious for the bare TiO_2 under the same treatment conditions (Figures 3d and S6). This is because that the decoration of Pt can greatly facilitate the H_2 dissociation and generation of more active hydrogen (H·), which correspondingly contributes to the more Ov generation on TiO_2 through reduction effect, resulting in the obvious color changes. To clearly verify the Ov generation after H_2 activation treatment, electron paramagnetic resonance (EPR) characterization that can provide the relative Ov content of the photocatalysts was conducted (Figure 3e). Similar with the color change tendency of the photocatalysts, the Ov content determined by peak intensity (at around g = 2.003) increases in the order of TiO_2 ≈ $Pt_{SA+NC}@TiO_2$ ≈ $Pt_{SA+NC}@TiO_2$-175R < $Pt_{SA+NC}@TiO_2$-300R < $Pt_{SA+NC}@TiO_2$-475R photocatalysts, indicating that the Ov content can be well modulated by facilely varying the activation temperatures. The changes of physicochemical properties also enhance the photo-adsorption property (Figure 3f) and the zeta potentials (Figure 3g). The enhanced photo-adsorption in the visible light region should be closely related to the nitrogen doping and formed Ov. The zeta potentials present a gradually increased tendency after decoration of Pt cocatalysts and the following activation, which may change the adsorption strength between reacting molecules and photocatalyst surfaces, and further influence the photocatalytic performance.

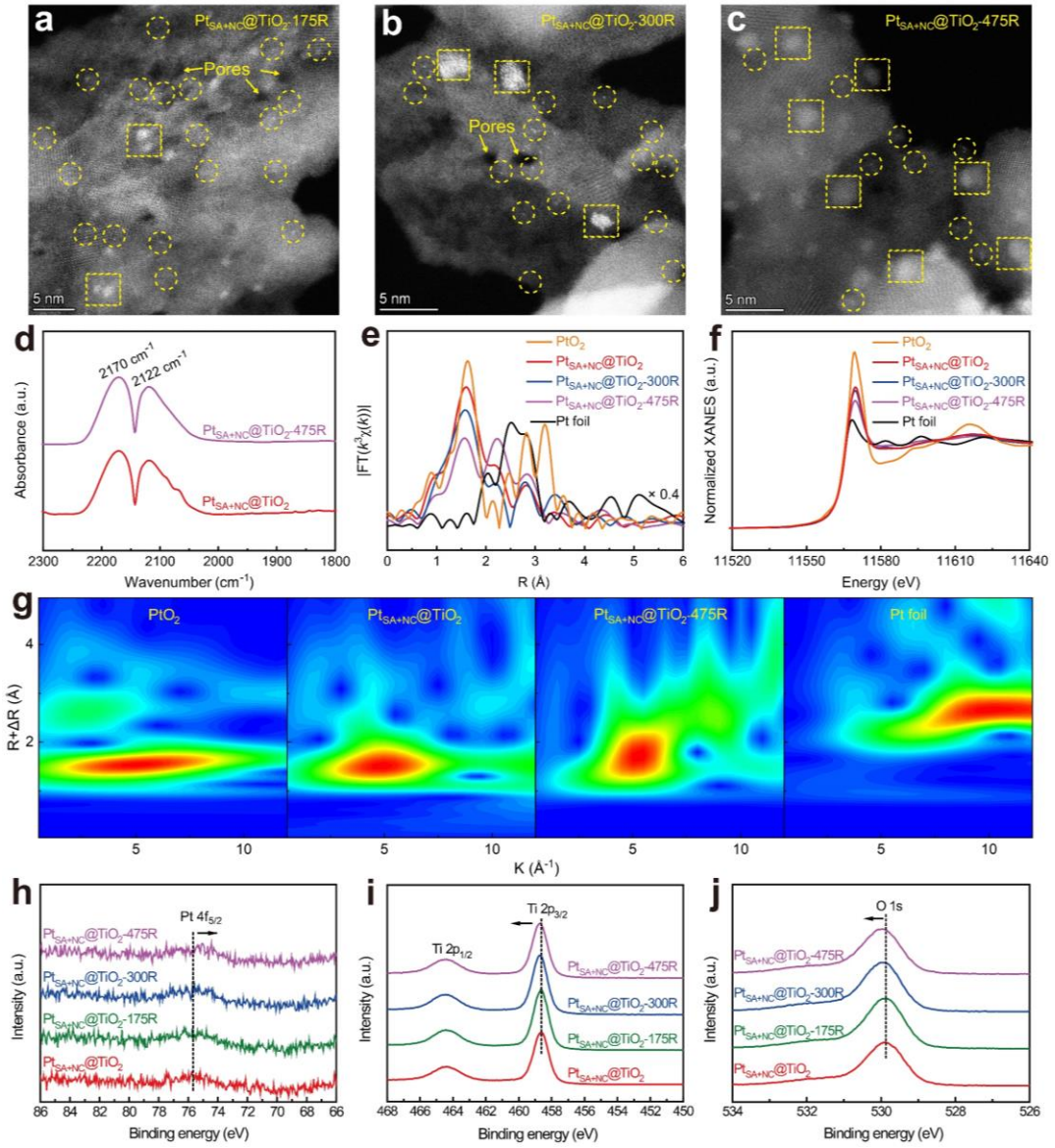

Figure 4. Structural and electronic properties of the activated photocatalysts. The HAADF-STEM images of the activated (a) $Pt_{SA+NC}@TiO_2$-175R, (b) $Pt_{SA+NC}@TiO_2$-300R and (c) $Pt_{SA+NC}@TiO_2$-475R photocatalysts. (d) CO-DRFITS spectra of the $Pt_{SA+NC}@TiO_2$ and representative $Pt_{SA+NC}@TiO_2$-475R photocatalysts. (e) Pt L_{III}-edge k^3-weighted EXAFS spectra and (f) normalized Pt L_{III}-edge XANES spectra of the photocatalysts and reference Pt foil and PtO_2. (g) WT-EXAFS spectra of $Pt_{SA+NC}@TiO_2$, $Pt_{SA+NC}@TiO_2$-475R photocatalysts, Pt foil and PtO_2. XPS (h) Pt 4f, (i) Ti 2p and (j) O 1s spectra of the photocatalysts.

Pt cocatalyst size and electronic property are the two main factors that influence the PHE performance. The variation of Pt cocatalyst size over the photocatalysts under activation treatment of various temperatures was characterized by HAADF-STEM (Figures 4a−c and S7−10). No obvious change is observed in view of the morphology and microstructure for the photocatalysts even under the high temperature activation

treatment (475 °C, Figures S9−11), indicating the good stability of the materials. From the HAADF-STEM image of the Pt_{SA+NC}@TiO_2-175R photocatalysts (Figure 4a), the SAs still account for a large proportion coexisting with some atomic clusters/nanoclusters with a mean size of *ca.* 0.97 nm, which is similar to that of the as-prepared counterparts (*ca.* 0.95 nm, Table S1). While the Pt nanoclusters with a mean size of *ca.* 1.20 nm can be observed for the Pt_{SA+NC}@TiO_2-475R photocatalysts, which still coexist with a certain number of SAs (Figure 4c). There is only a slight increase in view of the nanocluster size due to the stabilization effect of porous structure and rich Ov of TiO_2 toward Pt cocatalysts (This nearly could consider to be unchanged before and after activation considering experiment and measurement errors). While Ov content is obviously increased with increased activation temperatures (Figure 5b), and thus the enhanced Pt-Ov synergy, instead of the slight change of cluster size, should be the main reason that results in the activity enhancement. Moreover, the cocatalysts are still highly dispersed for the activated photocatalysts, which can be further confirmed by the XRD and CO-DRFITS characterizations. From the XRD patterns of the photocatalysts (Figure S12), the diffraction peak of Pt species is still not detected except the peaks of anatase TiO_2 due to the high dispersion. Additionally, the bridge-bonded peak at around 1865 cm^{-1} is also not detected from the CO-DRFITS spectrum of the Pt_{SA+NC}@TiO_2-475R photocatalyst (Figure 4d), suggesting that the NCs are quite different from the Pt NPs of the as-prepared Pt_{NP}@TiO_2 photocatalysts.

The atomically dispersed property of Pt cocatalysts can be further verified from the extended X-ray absorption fine structure (EXAFS, Figure 4e) spectra of the photocatalysts and reference Pt foil and PtO_2, i.e., obvious Pt−O peak at around 1.6 Å can be observed from the spectra of the photocatalysts, and the peak intensity gradually decreases with increased activation temperature. Especially for the Pt_{SA+NC}@TiO_2-475R photocatalysts, the peak at around 2.2 Å can be observed attributable to the Pt−Pt bond of small PtO_x clusters. The EXAFS fitting results also (Table S2) show that the coordination number of Pt−O in the photocatalysts decreases gradually with increased activation temperature. Besides, the EXAFS wavelet transform (WT) analysis also presents the consistent results (Figure 4g). From the WT contour plots, the intensity

maximum at *ca.* 5 and 10 $Å^{-1}$ can be assigned to the Pt−O and Pt−Pt coordination, respectively. To gain the detailed information of valence states and electronic structure of Pt cocatalysts, the normalized Pt L_{III}-edge X-ray absorption near-edge structure (XANES, Figure 4f) spectra of the photocatalysts were also given. Clearly the white-line peak intensity decreases in the following order: PtO_2 > $Pt_{SA+NC}@TiO_2$ > $Pt_{SA+NC}@TiO_2$-175R > $Pt_{SA+NC}@TiO_2$-300R > $Pt_{SA+NC}@TiO_2$-475R > Pt foil, indicating the gradually decreased valence states with the increased activation temperatures. The lower white-line intensity also indicates the higher electron filling of the Pt 5d orbital due to the electron transfer from TiO_2 to Pt, resulting in the electron-rich Pt sites.[54] As also confirmed by XPS characterization (Figures 4h−j and S13), the Pt 4f binding energies of the activated photocatalysts present the negative shifts compared with that of the as-prepared counterparts (Figure 4h), and correspondingly the binding energies of Ti 2p and O 1s shift to higher positions (Figures 4i and 4j), which again indicate the electron transfer from TiO_2 to Pt, resulting in the increased electron density (i.e., electron-rich state) of Pt for the activated photocatalysts. Notably, TiO_2 donates more electrons to Pt with increased temperatures and this should be related to the enhanced concentration of Ov. The electron transfer from TiO_2 to Pt adjusts the unoccupied Pt 5d orbital, exciting the electron-rich surface state and modifying interaction strength toward reacting molecules,[55] which would be beneficial for the enhancement of photocatalytic activity.

3.3. Evaluation of Photocatalytic Hydrogen Evolution Activity. The activities of the $Pt_{SA+NC}@TiO_2$ photocatalysts before and after H_2 activation treatment were tested by the PHE reactions. During the photocatalytic water splitting reaction, the activated three photocatalysts exhibit monotonely increased H_2 evolution activity with the increase of activation temperature and Ov content, which is much higher than that of the as-prepared $Pt_{SA+NC}@TiO_2$ photocatalysts (Figures 5a and 5b). Specifically, when the $Pt_{SA+NC}@TiO_2$ photocatalysts are activated at lower temperature (175 °C), the obtained $Pt_{SA+NC}@TiO_2$-175R photocatalysts present an increased activity with a TOF value of 2768 h^{-1}, which should be related to the decreased SA/NC ratio. The TOF value can be further enhanced to 3428 h^{-1} and 3645 h^{-1} when the photocatalysts are

activated at 300 and 475 °C respectively, which are much higher than that of the reported Pt-based photocatalysts (Table S3). The obtained wavelength-dependent apparent quantum efficiency (AQE) at 350 nm is 9.4% over the Pt_{SA+NC}@TiO_2-475R photocatalysts. The transient photocurrent response test results also present the consistent tendency (Figure 5c). Note that the curve shape of the Pt_{SA+NC}@TiO_2-475R photocatalysts is different from others: the photocurrent value is high at initial stage and then decrease keeping stable, probably due to the influence physicochemical properties of the photocatalysts such as color and Ov content (especially the Ov content induced change of charge trapping states).[40] As expected, the Pt_{SA+NC}@TiO_2-475R photocatalysts also exhibit the remarkably enhanced activity compared with the as-prepared counterparts in methanol dehydrogenation reaction (Figure S14). In addition, the tests of hydrolytic dehydrogenation of ammonia borane (AB, NH_3BH_3) over the catalysts were also performed. As shown in Figure 5d, the as-prepared Pt_{SA+NC}@TiO_2 and activated Pt_{SA+NC}@TiO_2-475R present almost the same H_2 evolution activities and H_2 is not completely released even when the reaction time reaches to 38 min under the dark conditions, suggesting that the structure changes (increased Pt size and Ov content) of the photocatalysts have little influence on the activity under the dark conditions. This is probably because that the high-dispersion Pt nanoclusters with small size and low content are not efficient for the activation of H_2O molecules, generally considered to be the rate-determining step (RDS) for the reaction. While the reaction can be rapidly completed in 9 min catalyzed by the Pt_{SA+NC}@TiO_2-475R under the light irradiation, which again exhibits much higher photocatalytic H_2 evolution activity than the Pt_{SA+NC}@TiO_2 (15 min). Note that bare TiO_2 is inactive for the hydrolytic reaction under the dark conditions, and both TiO_2 and TiO_2-475R still cannot release the stoichiometric H_2 even under the light irradiation. These results demonstrate the significant roles of Pt and Ov in synergistically boosting the PHE activity.

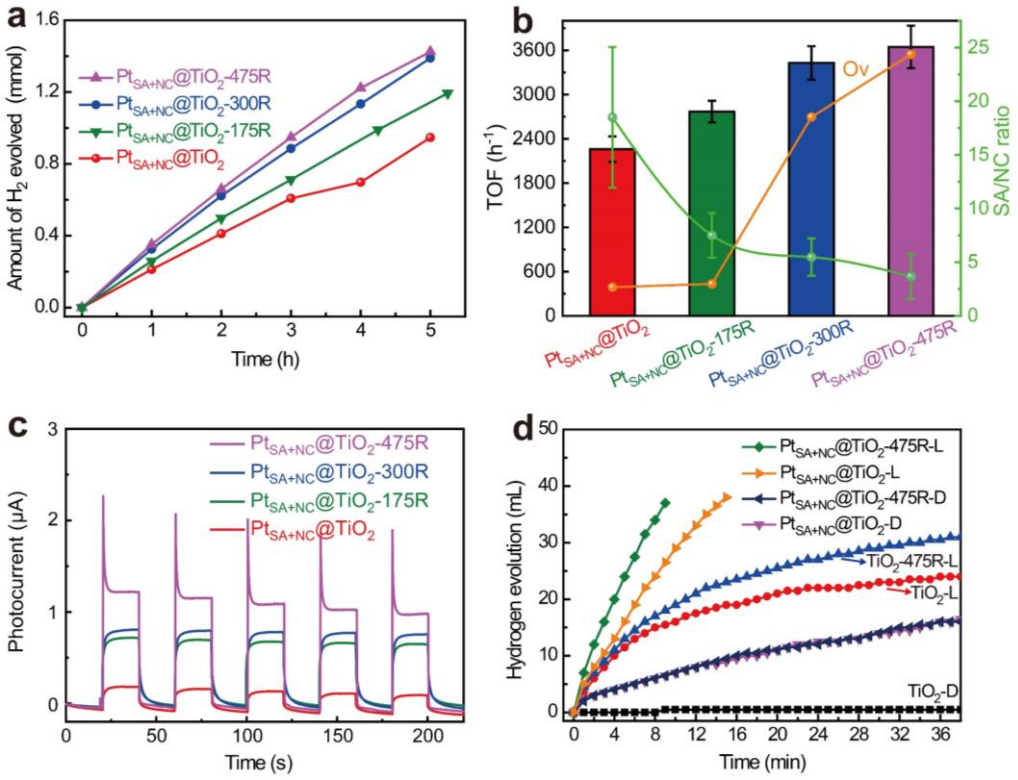

Figure 5. PHE activity evaluation of the photocatalysts. (a) The continuous profiles of photocatalytic H_2 evolution (20 vol% methanol−aqueous) of the photocatalysts under UV−Vis light irradiation. (b) The corresponding TOF value, SA/NC ratio and Ov content of the photocatalysts. (c) The transient photocurrent responses of the photocatalysts. (d) The continuous H_2 evolution profiles from AB solution (0.05 mol/L AB, 30 °C) over the photocatalysts under dark (D) and UV−Vis light (L) irradiation.

3.4. Charge Transfer−Separation Efficiency of the Photocatalysts. To verify the enhanced carrier dynamics due to the potential Pt−Ov interfacial sites, photoluminescence (PL) spectra, transient photocurrent and electrochemical impedance spectroscopy (EIS) measurements were performed. The PL intensity shows the decreased tendency after the decoration of Pt cocatalysts and further activation treatment (Figure 6a), and especially the $Pt_{SA+NC}@TiO_2$-475R photocatalysts present the lowest radiative recombination quenching signal of photogenerated electron-hole pairs, indicating the most efficient charge separation efficiency of the photocatalysts. This can be further verified by the transient photocurrent response (Figure 5c) and EIS (Figure S15) results, from which the $Pt_{SA+NC}@TiO_2$-475R photocatalysts present the highest photocurrent density and smallest arc radius due to the enhanced charge separation efficiency and much-decreased interfacial charge transfer resistance, respectively. It is the enhanced charge transfer-separation efficiency due to the unique

interfacial electric field and suitable Ov content that contribute to the boosted PHE activity (Figures 6b and S16). Additionally, the charge transfer dynamics of the representative three photocatalysts were further investigated by ultrafast transient absorption (TA) spectroscopy. From the spectrum of pristine TiO_2 (Figure 6c), the positive TA signal corresponding to photoexcited electrons was probed at wavelength of longer than 400 nm and picosecond timescale. While the deposition of Pt cocatalysts ($Pt_{SA+NC}@TiO_2$) and the further activation treatment ($Pt_{SA+NC}@TiO_2$-475R) result in the negative bleach signals below the wavelengths of 466 and 475 nm respectively, which should be ascribed to the electron depletion caused by the interband and/or interface transition.[42,56] Similar results can be obtained from the 2D contour plots of the three photocatalysts (Figures 6d−f). In addition, the decay kinetics of the photocatalysts were also monitored and analyzed (Figures 6g−i). The results show that the time constants of the photocatalysts present the monotonely decreased tendency after Pt deposition and further activation treatment, again indicating the ultrafast electron capture on Pt and Pt-Ti^{3+}-Ov interface sites.[56] These results indicate that the constructed interfacial electric fields are responsible for the efficient charge separation and the potential reactive sites.

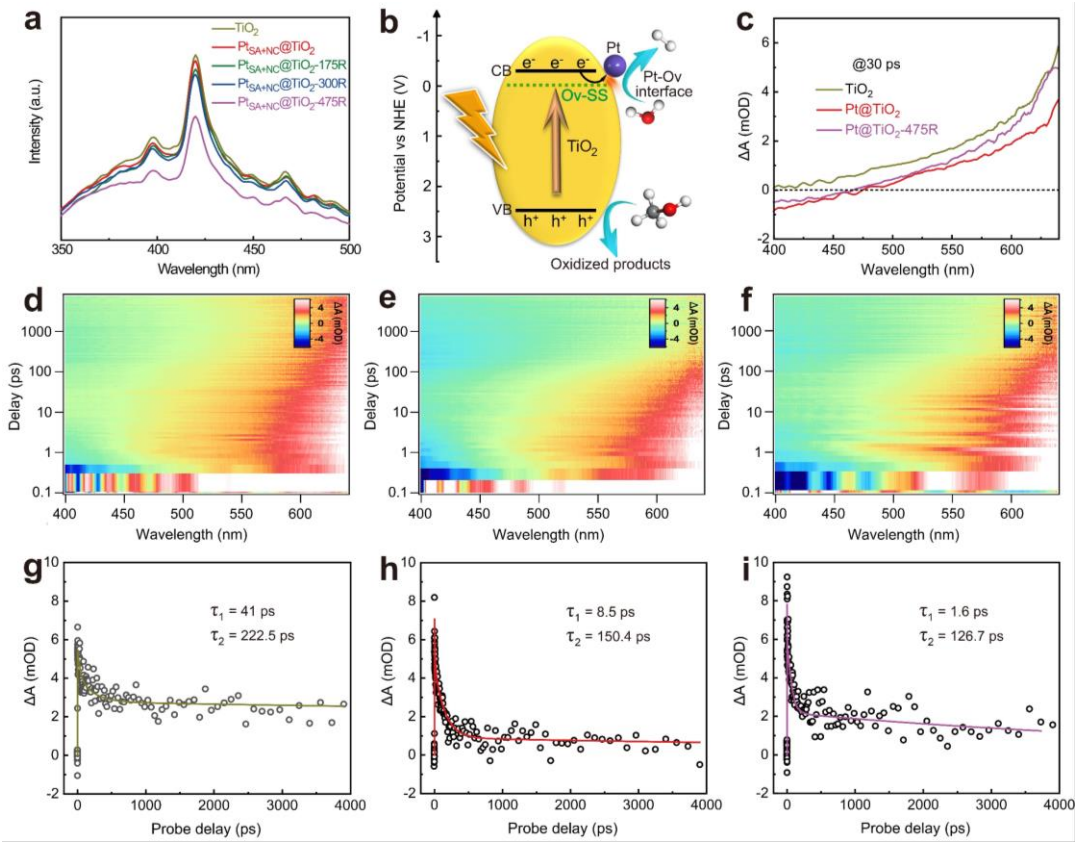

Figure 6. The charge transfer−separation efficiency of the photocatalysts. (a) PL spectra of the photocatalysts. (b) The potential reaction mechanism (SS represents shallow state). (c) 2D contour plots of TA spectra of the representative (d) TiO_2, (e) $Pt_{SA+NC}@TiO_2$ and (f) $Pt_{SA+NC}@TiO_2$-475R photocatalysts at 350 nm excitation, and the corresponding TA decay kinetics probed at 630 nm for the (g) TiO_2, (h) $Pt_{SA+NC}@TiO_2$ and (i) $Pt_{SA+NC}@TiO_2$-475R photocatalysts.

3.5. Mechanistic Insights into the SA−NC−Ov Synergy. The H_2O adsorption−dissociation and H_2 desorption are the significant steps in the whole water splitting process. Therefore, H_2O and H_2 temperature-programmed-desorption (TPD) experiments were conducted to probe the interaction between the reaction molecules and the photocatalyst surfaces. From the mass spectra of H_2O-TPD (Figure 7a), the desorption temperature of H_2O on bare TiO_2 photocatalysts is approximately 224 °C, and the decoration of Pt cocatalysts leads to the increased desorption temperature (*ca.* 245 °C). Interestingly, the desorption temperatures begin to decrease gradually with the increased activation temperatures, indicating a weakening interaction between H_2O molecules and the photocatalyst surfaces. It should be noted that the areas of desorption peak, corresponding to the adsorbed amounts of H_2O, are similar before and after Pt decoration, indicating that TiO_2 serves as the main adsorption site for H_2O molecules.

However, the desorption peak areas present an increased tendency for the further activated photocatalysts, which should be ascribed to the new Ov formation contributing to the adsorption of H_2O. Moreover, H_2-TPD experiments were also conducted (Figure 7b) to probe the desorption of H_2 products from the photocatalyst surfaces. For the bare TiO_2 photocatalysts, a weak peak is detected at low temperature region (*ca.* 78 °C), which should be attributed to the physically adsorbed hydrogen. For the as-prepared $Pt_{SA+NC}@TiO_2$ photocatalysts, two additional weak peaks appear on the profile at around 150 and 413 °C, respectively, which can be assigned to reversibly chemisorbed hydrogen (Pt−H interactions) and irreversible hydrogen.[57] Notably, only the reversible Pt−H peaks are observed for the three activated photocatalysts, and the corresponding desorption peaks gradually shift to lower temperatures with increased activation temperatures. This observation indicates a weakening Pt−H bond interaction and easier desorption of hydrogen from the photocatalyst surfaces.

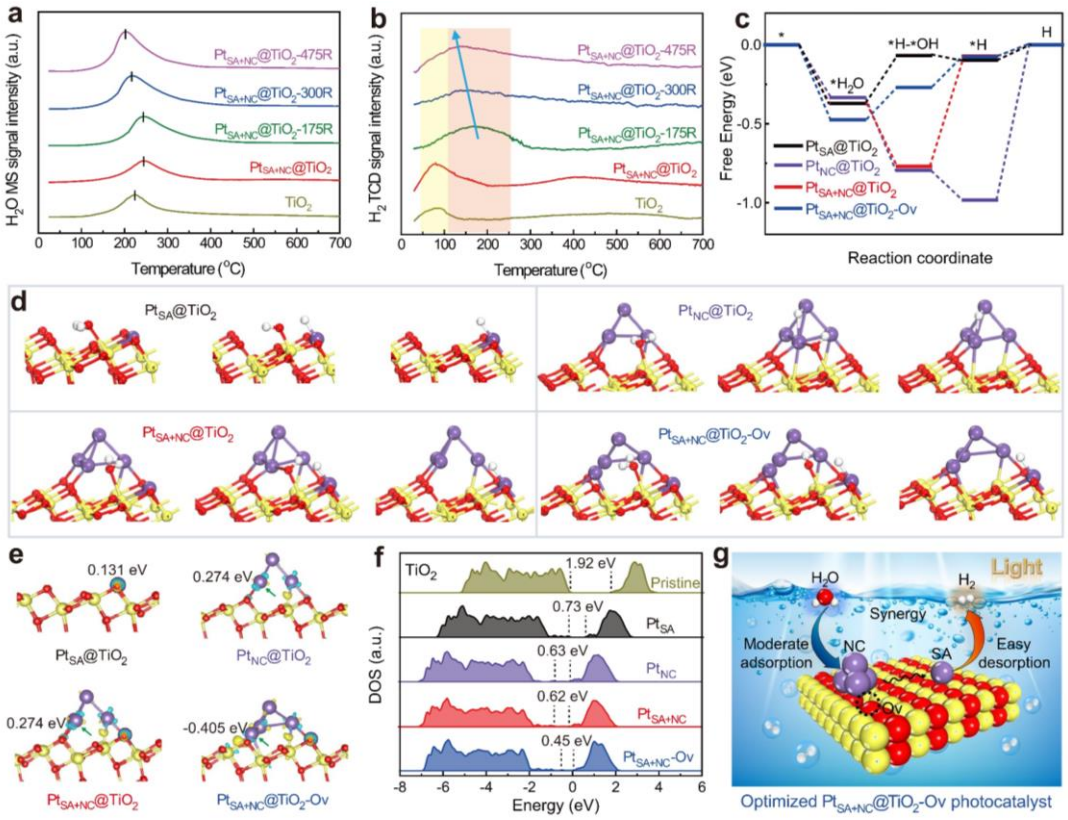

Figure 7. TPD and DFT calculation results. (a) H_2O-TPD and (b) H_2-TPD profiles of the photocatalysts. (c) Free energy diagrams for water splitting process over the photocatalysts. (d) The configuration of *H_2O, *H−*OH and *H on the TiO_2 confined $Pt_{SA}@TiO_2$, $Pt_{NC}@TiO_2$, $Pt_{SA+NC}@TiO_2$ and $Pt_{SA+NC}@TiO_2$-Ov (i.e., $Pt_{SA+NC}@TiO_2$-R) photocatalysts. (e) Three-dimensional charge density difference of Pt on the photocatalysts with isosurface value of 0.03 eV·Å^{-3}. Electron

accumulation is yellow and depletion is blue. (f) Total DOS of TiO_2 for the photocatalysts. (g) Schematics of synergistic photocatalytic mechanism over the Pt SA−NC−Ov sites. Red, yellow, purple and white spheres depict O, Ti, Pt and H atoms, respectively.

To gain detailed and deep insights into the respective roles of Pt SA, NC and Ov in the reaction and their synergistic catalytic mechanisms, DFT calculations were further performed. We constructed oxygen vacancies at different positions on the TiO_2 surface and identified the most stable structure for Pt loading (Figure S17). Figure 7d presents the optimized configurations of *H_2O, *H−*OH and *H on the TiO_2(101) facet and the corresponding decorated Pt_{SA} (Pt_1), Pt_{NC} (Pt_4), Pt_{SA+NC} (Pt_1−Pt_4) and Pt_{SA+NC}-Ov (Pt_1−Pt_4−Ov) photocatalysts (also see Figures S18 and 19). H_2O molecule can be stably adsorbed on the TiO_2 (Ti sites), and this is consistent with the above H_2O-TPD results, i.e., TiO_2 is the potential adsorption and reaction sites of H_2O molecule. The introduction of Pt_{SA} cocatalysts has limited influence on the reaction efficiency in the present photocatalytic system, and this is because that the dissociation of H_2O molecule on Pt_{SA}@TiO_2 is an uphill process (0.3 eV energy barrier from Figure 7c). Although Pt_{SA} is unfavorable for the dissociation of H_2O molecule, *H desorption on Pt_{SA} is quite easy to occur, again demonstrating that the Pt_{SA} is the potential desorption site of H_2 molecule. The dissociation of H_2O molecule (into *OH and *H) on Pt_{NC}@TiO_2, a spontaneous downhill process, is quite easier due to the lowered the dissociation energy barrier, again demonstrating that the larger size Pt_{NC} could be the perfect adsorption–dissociation sites of H_2O molecule. However, *H desorption from Pt_{NC} is quite difficult needing to overcome a much higher energy barrier (0.98 eV). As expected, for the coexisted Pt_{SA+NC}@TiO_2 photocatalysts combining the advantages of Pt_{SA}@TiO_2 and Pt_{NC}@TiO_2, the case seems to achieve a trade-off optimization. The dissociation of H_2O molecule on Pt_{SA+NC}@TiO_2 is a spontaneous downhill process, and *H desorption also becomes quite easy. However, the *H generation from the dissociation of *H−*OH intermediate becomes the RDS due to the strong Pt_{NC}−*OH bonding. Impressively, this can be well addressed by further introducing Ov on the adjacent Pt_{NC} site, which makes the whole reaction process achieve the energy-optimal states. The introduced Ov makes the adjacent Pt atom form a new bond with Ti atom (Figure 7d), and correspondingly

weakens the adsorption toward *OH intermediate, thus shifting the adsorption energy to a medium value. Considering the possible existence of Ov in the sub-surface, we also analyzed the impact of sub-surface Ov on adsorption energy (Figure S20). The results demonstrate that Ov preferentially migrates from the sub-surface to the surface during the reaction process, consistent with previous studies, indicating that molecular adsorption efficiently facilitates the diffusion of Ov from the sub-surface layer to the surface.[58,59] Consequently, we hypothesize that Ov in the sub-surface could similarly influence the reaction mechanism as surface Ov. The Gibbs reaction energy profiles for methanol reforming on the $Pt_{SA+NC}@TiO_2$-Ov photocatalysts were also calculated to explore the impact of methanol on the hydrogen production process (Figure S21).[43] The results indicate that the product of methanol reforming after dehydrogenation adsorbs too strongly on the catalyst surface, hindering the occurrence of the reaction. Nevertheless, due to the lower energy barrier of *H-*CH_2OH formation compared to *H-OH, methanol may serve as a hydrogen donor, synergistically promoting the hydrogen production.[60,61]

To investigate the underlying factors influencing the adsorption energy modulation, the electronic structures of the photocatalysts were analyzed, including the charge density difference and density of state (DOS). As presented in Figures 7e, S22 and S23, the introduction of Pt NC has a negligible influence on the electropositive property of Pt SA with only a slight decrease from 0.131 to 0.115 eV. However, the introduction of Ov changes the coordination environment of Pt atom in the nanocluster, leading to a change in bonding from Pt−O to Pt−Ti for the Pt atom located at the bottom (as pointed by the arrow). This transition transforms the electropositive Pt atom (Bader charge: +0.274e) into electronegative Pt atom (Bader charge: −0.405e), consequently weakening the bonding with electronegative *OH. Figure 7f illustrates the total DOS of TiO_2 for the various photocatalysts. Obviously, the introduction of Pt SA or/and NC narrows the band gap of TiO_2, which is further enhanced by introducing Ov, consistent with the above UV−Vis results (Figure 3f). Moreover, the DOS of Pt SA and Pt NC in $Pt_{SA}@TiO_2$, $Pt_{SA+NC}@TiO_2$ and $Pt_{SA+NC}@TiO_2$-Ov photocatalysts were also given in Figure S24. It is evident that the introduction of Pt NC causes the downshift of the d-

band center of Pt SA (Figure S24a), resulting in weakened bond interaction with H and enhanced H_2 evolution activity. The desorption of *OH intermediate on $Pt_{SA+NC}@TiO_2$ is the RDS, therefore, the interaction between Pt_{SA+NC} and *OH was also investigated via DOS calculations (Figure S25a). The Pt 5d orbital of Pt_{NC} and O 2p orbital of *OH exhibit a strong hybridization effect, while this effect is significantly weakened over the $Pt_{SA+NC}@TiO_2$-Ov, indicating the easier desorption of *OH intermediate (Figure S25b). The relatively easier *OH desorption from the active sites alleviates the site-blocking effect and releases more active sites, contributing to the high-efficiency PHE activity.[62] These results strongly support the indispensable roles of Pt SA, NC and Ov in achieving high-efficiency H_2O splitting (Figure 7g), and highlight the integrated synergies of the species in boosting the PHE activity.

The activation treatment results in the slightly increased cocatalyst size and prominently increased Ov content in the present photocatalyst systems. The activated photocatalysts exhibit remarkably boosted PHE activity, the following several factors should account for this phenomenon. Firstly, the activated Pt NCs still present both the atomic dispersion and certain metallic property, which can well facilitate the adsorption−dissociation of H_2O molecules with the assistance of the newly formed Ov promoted by the strong H_2 dissociation and H· spillover capability; and meanwhile Pt NCs make the d-band center of Pt SAs downshifted resulting in the weakened bond interaction with H. Secondly, Pt SAs provide the high-efficiency desorption sites for H_2 molecules. Thirdly, the newly formed Ov can contribute to the photo-adsorption and charge separation acting as the potential electron-shuttling sites, and afford the adsorption sites for H_2O molecules. Moreover, Ov can modulate the electronic property of adjacent Pt NCs optimizing the bonding with electronegative *OH intermediates. Besides, the Ov can also well stabilize the Pt cocatalysts through metal−support strong interaction (Figure S26), resulting in the limited size increase of Pt NCs even after the high-temperature treatment. These factors caused by the remarkable SA−NC−Ov synergy account for the boosted PHE activity. The present investigation results strongly demonstrate the significance of species heterogeneity and their synergies in the PHE reactions involving multiple steps, and the insight revealed here will afford new

guidance for the rational design of atomically dispersed photocatalysts.

4. CONCLUSIONS

In summary, we have achieved the atomically dispersed Pt-based photocatalysts with tunable cocatalyst sizes and Ov concentrations by combining ALD and the following hydrogen activation strategy. The activated Pt_{SA+NC}@TiO_2-475R photocatalysts with high-dispersion Pt cocatalysts and rich Ovs exhibit a much higher TOF value of 3645 h^{-1} than as-prepared counterparts. Experimental and theoretical results reveal that the synergy of Pt SA, NC and adjacent Ov prominently boosts the photocatalytic activity: Pt NC facilitates the adsorption−dissociation of H_2O molecules adsorbed on the Ti sites, the adjacent Ov modifies electronic energy distribution of Pt NC and correspondingly optimize the adsorption toward the key intermediate *OH, and *H efficiently desorbs from Pt SA sites with the assistance of NCs. Ov can well stabilize the Pt cocatalysts during the activation process, and the existence of Pt contributes to the more Ov generation constructing high-efficiency Pt_{SA+NC}-Ov-Ti^{3+} interfacial sites boosting the PHE activity. The insights unraveled here demonstrate the significance of active site heterogeneity and their synergies in photocatalytic evolution reactions, and the design concept could be potentially extended to other cocatalyst−semiconductor photocatalytic systems.

Author contributions

[#] J. Zhang and P. Qiao contributed equally to this work.

Notes

The authors declare no competing financial interest.

ASSOCIATED CONTENT

Supporting Information

Computational modeling details and partial results; Experimental details, additional characterization data and catalytic performance tests (PDF)

ACKNOWLEDGEMENTS

We appreciate the financial support from the National Natural Science Foundation of China (22372130, 22102131 and 22208374), Fundamental Research Funds for the Central Universities (G2023KY0605 and 24GH0201184). We appreciate Dr. Dan Feng of Analytical & Testing Center of Northwestern Polytechnical University for HAADF-STEM measurements, and Shanghai Synchrotron Radiation Facility for XAFS measurements (beamline BL14W1). The authors also thank the beamline BL20U (Shanghai Synchrotron Radiation Facility) for providing the TEM testing time.

REFERENCES

(1) Takata, T.; Jiang, J.; Sakata, Y.; Nakabayashi, M.; Shibata, N.; Nandal, V.; Seki, K.; Hisatomi, T.; Domen, K. Photocatalytic water splitting with a quantum efficiency of almost unity. *Nature* **2022**, *581*, 411−414.

(2) Yao, S.; Zhang, X.; Zhou, W.; Gao, R.; Xu, W.; Ye, Y.; Lin, L.; Wen, X.; Liu, P.; Chen, B.; Crumlin, E.; Guo, J.; Zuo, Z.; Li, W.; Xie, J.; Lu, L.; Kiely, C. J.; Gu, L.; Shi, C.; Rodriguez, J. A.; Ma, D. Atomic-layered Au clusters on α-MoC as catalysts for the low-temperature water-gas shift reaction. *Science* **2017**, *357*, 389−393.

(3) Lee, C. W.; Lee, B.-H.; Park, S.; Jung, Y.; Han, J.; Heo, J.; Lee, K.; Ko, W.; Yoo, S.; Bootharaju, M. S.; Ryu, J.; Nam, K. T.; Kim, M.; Hyeon, T. Photochemical tuning of dynamic defects for high-performance atomically dispersed catalysts. *Nat. Mater.* **2024**, *23*, 552–559.

(4) Martin, D. J.; Liu, G.; Moniz, S. J.; Bi, Y.; Beale, A. M.; Ye, J.; Tang, J. Efficient visible driven photocatalyst, silver phosphate: performance, understanding and perspective. *Chem. Soc. Rev.* **2015**, *44*, 7808−7828.

(5) Ran, J.; Zhang, J.; Yu, J.; Jaroniec, M.; Qiao, S. Z. Earth-abundant cocatalysts for semiconductor-based photocatalytic water splitting. *Chem. Soc. Rev.* **2014**, *43*, 7787−7812.

(6) Zhang, N.; Qi, M. Y.; Yuan, L.; Fu, X.; Tang, Z. R.; Gong, J.; Xu, Y. J. Broadband light harvesting and unidirectional electron flow for efficient electron accumulation for hydrogen generation. *Angew. Chem. Int. Ed.* **2019**, *131*, 10108−10112.

(7) Guo, Y.; Zhou, Q.; Nan, J.; Shi, W.; Cui, F.; Zhu, Y. Perylenetetracarboxylic acid nanosheets with internal electric fields and anisotropic charge migration for photocatalytic hydrogen evolution. *Nat. Commun.* **2022**, *13*, 2067.

(8) Yang, J.; Wang, D.; Han, H.; Li, C. Roles of cocatalysts in photocatalysis and photoelectrocatalysis. *Acc. Chem. Res.* **2013**, *46*, 1900−1909.

(9) Zeng, L.; Xue, C. Single metal atom decorated photocatalysts: Progress and challenges. *Nano Research* **2021**, *14*, 934−944.

(10) Chen, Y.; Ji, S.; Sun, W.; Lei, Y.; Wang, Q.; Li, A.; Chen, W.; Zhou, G.; Zhang, Z.; Wang, Y.; Zheng, L.; Zhang, Q.; Gu, L.; Han, X.; Wang, D.; Li, Y. Engineering the atomic interface with single platinum atoms for enhanced photocatalytic hydrogen production. *Angew. Chem. Int. Ed.* **2020**, *132*, 1311−1317.

(11) Zhang, Y.; Zhao, J.; Wang, H.; Xiao, B.; Zhang, W.; Zhao, X.; Lv, T.; Thangamuthu, M.; Zhang, J.; Guo, Y.; Ma, J.; Lin, L.; Tang, J.; Huang, R.; Liu, Q. Single-atom Cu anchored catalysts for photocatalytic

renewable H_2 production with a quantum efficiency of 56%. *Nat. Commun.* **2022**, *13*, 58.
(12) Wang, Y.; Qin, S.; Denisov, N.; Kim, H.; Badura, Z.; Sarma, B. B.; Schmuki, P. Reactive deposition versus strong electrostatic adsorption (SEA): A key to highly active single atom co-catalysts in photocatalytic H_2 generation. *Adv. Mater.* **2023**, *35*, 2211814.
(13) Qin, S.; Denisov, N.; Will, J.; Kolařík, J.; Schmuki, P. A few Pt single atoms are responsible for the overall co-catalytic activity in Pt/TiO_2 photocatalytic H_2 generation. *Sol. RRL* **2022**, *6*, 2101026.
(14) Zhang, Y.; Xu, Z.; Li, G.; Huang, X.; Hao, W.; Bi, Y. Direct observation of oxygen vacancy self-healing on TiO_2 photocatalysts for solar water splitting. *Angew. Chem. Int. Ed.* **2019**, *58*, 14229−14233.
(15) Hang Li, Y.; Xing, J.; Jia Chen, Z.; Li, Z.; Tian, F.; Rong Zheng, L.; Feng Wang, H.; Hu, P.; Jun Zhao, H.; Yang, H. G. Unidirectional suppression of hydrogen oxidation on oxidized platinum clusters. *Nat. Commun.* **2013**, *4*, 2500.
(16) Lan, K.; Wang, R.; Wei, Q.; Wang, Y.; Hong, A.; Feng, P.; Zhao, D. Stable Ti^{3+} defects in oriented mesoporous titania frameworks for efficient photocatalysis. *Angew. Chem. Int. Ed.* **2020**, *132*, 17829−17836.
(17) Xiao, M.; Zhang, L.; Luo, B.; Lyu, M.; Wang, Z.; Huang, H.; Wang, S.; Du, A.; Wang, L. Molten-salt-mediated synthesis of an atomic nickel co-catalyst on TiO_2 for improved photocatalytic H_2 evolution. *Angew. Chem. Int. Ed.* **2020**, *132*, 7297−7301.
(18) Ge, X.; Zhou, P.; Zhang, Q.; Xia, Z.; Chen, S.; Gao, P.; Zhang, Z.; Gu, L.; Guo, S. Palladium single atoms on TiO_2 as a photocatalytic sensing platform for analyzing the organophosphorus pesticide chlorpyrifos. *Angew. Chem. Int. Ed.* **2020**, *132*, 238−242.
(19) Lee, W. H.; Lee, C. W.; Cha, G. D.; Lee, B.-H.; Jeong, J. H.; Park, H.; Heo, J.; Bootharaju, M. S.; Sunwoo, S.-H.; Kim, J. H. Floatable photocatalytic hydrogel nanocomposites for large-scale solar hydrogen production. *Nat. Nanotech.* **2023**, *18*, 754−762.
(20) Dong, C.; Lian, C.; Hu, S.; Deng, Z.; Gong, J.; Li, M.; Liu, H.; Xing, M.; Zhang, J. Size-dependent activity and selectivity of carbon dioxide photocatalytic reduction over platinum nanoparticles. *Nat. Commun.* **2018**, *9*, 1252.
(21) Liu, Y.; Yang, W.; Chen, Q.; Cullen, D. A.; Xie, Z.; Lian, T. Pt particle size affects both the charge separation and water reduction efficiencies of CdS−Pt nanorod photocatalysts for light driven H_2 generation. *J. Am. Chem. Soc.* **2022**, *144*, 2705−2715.
(22) Wu, X.; Zhang, H.; Dong, J.; Qiu, M.; Kong, J.; Zhang, Y.; Li, Y.; Xu, G.; Zhang, J.; Ye, J. Surface step decoration of isolated atom as electron pumping: Atomic-level insights into visible-light hydrogen evolution. *Nano Energy* **2018**, *45*, 109−117.
(23) Shahrezaei, M.; Hejazi, S. M. H.; Kmentova, H.; Sedajova, V.; Zboril, R.; Naldoni, A.; Kment, S. Ultrasound-driven defect engineering in TiO_{2-x} nanotubes toward highly efficient platinum single atom enhanced photocatalytic water splitting. *ACS Appl. Mater. Interfaces* **2023**, 15, 37976−37985.
(24) Hejazi, S.; Mohajernia, S.; Osuagwu, B.; Zoppellaro, G.; Andryskova, P.; Tomanec, O.; Kment, S.; Zbořil, R.; Schmuki, P. On the controlled loading of single platinum atoms as a co-catalyst on TiO_2 anatase for optimized photocatalytic H_2 generation. *Adv. Mater.* **2020**, *32*, 1908505.
(25) Fang, X.; Shang, Q.; Wang, Y.; Jiao, L.; Yao, T.; Li, Y.; Zhang, Q.; Luo, Y.; Jiang, H. L. Single Pt atoms confined into a metal−organic framework for efficient photocatalysis. *Adv. Mater.* **2018**, *30*, 1705112.
(26) Yan, J.; Ji, Y.; Batmunkh, M.; An, P.; Zhang, J.; Fu, Y.; Jia, B.; Li, Y.; Liu, S.; Ye, J.; Ma, T. Breaking platinum nanoparticles to single-atomic Pt-C_4 co-catalysts for enhanced solar-to-hydrogen conversion. *Angew. Chem. Int. Ed.* **2021**, *60*, 2541−2547.

(27) Li, X.; Bi, W.; Zhang, L.; Tao, S.; Chu, W.; Zhang, Q.; Luo, Y.; Wu, C.; Xie, Y. Single-atom Pt as co-catalyst for enhanced photocatalytic H_2 evolution. *Adv. Mater.* **2016**, *28*, 2427−2431.
(28) Gao, C.; Low, J.; Long, R.; Kong, T.; Zhu, J.; Xiong, Y. Heterogeneous single-atom photocatalysts: fundamentals and applications. *Chem. Rev.* **2020**, *120*, 12175−12216.
(29) Zhu, Y.; Tian, P.; Jiang, H.; Mu, J.; Meng, L.; Su, X.; Wang, Y.; Lin, Y.; Zhu, Y.; Song, L.; Li, C. Synergistic effect of platinum single atoms and nanoclusters boosting electrocatalytic hydrogen evolution. *CCS Chem.* **2021**, *3*, 2539−2547.
(30) Liu, P.; Huang, Z.; Gao, X.; Hong, X.; Zhu, J.; Wang, G.; Wu, Y.; Zeng, J.; Zheng, X. Synergy between palladium single atoms and nanoparticles via hydrogen spillover for enhancing CO_2 photoreduction to CH_4. *Adv. Mater.* **2022**, *34*, 2200057.
(31) Zhang, J.; Pan, Y.; Feng, D.; Cui, L.; Zhao, S.; Hu, J.; Wang, S.; Qin, Y. Mechanistic insight into the synergy between platinum single atom and cluster dual active sites boosting photocatalytic hydrogen evolution. *Adv. Mater.* **2023**, *35*, 2300902.
(32) Zhang, J.; Zheng, X.; Yu, W.; Feng, X.; Qin, Y. Unravelling the synergy in platinum-nickel bimetal catalysts designed by atomic layer deposition for efficient hydrolytic dehydrogenation of ammonia borane. *Appl. Catal. B Environ.* **2022**, *306*, 121116.
(33) Xi, S.; Zhang, J.; Xie, K. Low-temperature water-gas shift reaction enhanced by oxygen vacancies in Pt-loaded porous single-crystalline oxide monoliths. *Angew. Chem. Int. Ed.* **2022**, *134*, e202209851.
(34) Zhang, J.; Wang, M.; Gao, Z.; Qin, X.; Xu, Y.; Wang, Z.; Zhou, W.; Ma, D. Importance of species heterogeneity in supported metal catalysts. *J. Am. Chem. Soc.* **2022**, *144*, 5108−5115.
(35) Zhang, X.; Zhang, M.; Deng, Y.; Xu, M.; Artiglia, L.; Wen, W.; Gao, R.; Chen, B.; Yao, S.; Zhang, X.; Peng, M.; Yan, J.; Li, A.; Jiang, Z.; Gao, X.; Cao, S.; Yang, C.; Kropf, A. J.; Shi, J.; Xie, J.; Bi, M.; Bokhoven, J. A.; Li, Y.-W.; Wen, X.; Flytzani-Stephanopoulos, M.; Shi, C.; Zhou, W.; Ma, D. A stable low-temperature H_2-production catalyst by crowding Pt on α-MoC. *Nature* **2021**, *589*, 396−401.
(36) Pan, Y.; Ma, X.; Wang, M.; Yang, X.; Liu, S.; Chen, H.-C.; Zhuang, Z.; Zhang, Y.; Cheong, W.-C.; Zhang, C.; Cao, X.; Shen, R.; Xu, Q.; Zhu, W.; Liu, Y.; Wang, X.; Zhang, X.; Yan, W.; Li, J.; Chen, H. M.; Chen, C.; Li, Y. Construction of N, P co-doped carbon frames anchored with Fe single atoms and Fe_2P nanoparticles as a robust coupling catalyst for electrocatalytic oxygen reduction, *Adv. Mater.* **2022**, *34*, 2203621.
(37) Zhu, Y.; Fan, K.; Hsu, C. S.; Chen, G.; Chen, C.; Liu, T.; Lin, Z.; She, S.; Li, L.; Zhou, H.; Zhu, Y.; Chen, H. M.; Huang, H. Supported ruthenium single-atom and clustered catalysts outperform benchmark Pt for alkaline hydrogen evolution. *Adv. Mater.* **2023**, *35*, 2301133.
(38) Wei, X.; Wen, X.; Liu, Y.; Chen, C.; Xie, C.; Wang, D.; Qiu, M.; He, N.; Zhou, P.; Chen, W.; Cheng, J.; Lin, H.; Jia, J.; Fu, X.-Z.; Wang S. Oxygen vacancy-mediated selective C−N coupling toward electrocatalytic urea synthesis. *J. Am. Chem. Soc.* **2022**, *144*, 11530−11535.
(39) Ai, M.; Zhang, J. W.; Wu, Y. W.; Pan, L.; Shi, C.; Zou, J. J. Role of vacancies in photocatalysis: a review of recent progress. *Chem.−Asian J.* **2020**, *15*, 3599−3619.
(40) Huang, Y.; Yu, Y.; Yu, Y.; Zhang, B. Oxygen vacancy engineering in photocatalysis. *Solar RRL* **2020**, *4*, 2000037.
(41) Hao, L.; Huang, H.; Zhang, Y.; Ma, T. Oxygen vacant semiconductor photocatalysts. *Adv. Funct. Mater.* **2021**, *31*, 2100919.
(42) An, X.; Wei, T.; Ding, P.; Liu, L.-M.; Xiong, L.; Tang, J.; Ma, J.; Wang, F.; Liu, H.; Qu, J. Sodium-directed photon-induced assembly strategy for preparing multisite catalysts with high atomic utilization efficiency. *J. Am. Chem. Soc.* **2023**, *145*, 1759−1768.

(43) Hejazi, S. M. H.; Shahrezaei, M.; Błoński, P.; Allieta, M.; Sheverdyaeva, P. M.; Moras, P.; Badura, Z.; Kalytchuk, S.; Mohammadi, E.; Zbořil, R.; Kment, Š.; Otyepka, M.; Naldoni, A.; Fornasiero, P. Defect engineering over anisotropic brookite toward substrate-specific photo-oxidation of alcohols. *Chem. Catal.* **2022**, *2*, 1177−1190.
(44) Fonseca, J.; Lu, J. Single-atom catalysts designed and prepared by the atomic layer deposition technique. *ACS Catal.* **2021**, *11*, 7018−7059.
(45) Knez, M.; Nielsch, K.; Niinistö, L. Synthesis and surface engineering of complex nanostructures by atomic layer deposition. *Adv. Mater.* **2007**, *19*, 3425−3438.
(46) Zhou, Z.; Wang, T.; Hu, T.; Xu, H.; Cui, L.; Xue, B.; Zhao, X.; Pan, X.; Yu, S.; Li, H.; Qin, Y.; Zhang, J.; Ma, L.; Liang, R.; Tan, C. Synergistic interaction between metal single-atoms and defective WO_{3-x} nanosheets for enhanced sonodynamic cancer therapy, *Adv. Mater.* **2024**, *36*, 2311002.
(47) Zhang, H.; Zuo, S.; Qiu, M.; Wang, S.; Zhang, Y.; Zhang, J.; Lou, X. W. Direct probing of atomically dispersed Ru species over multi-edged TiO_2 for highly efficient photocatalytic hydrogen evolution. *Sci. Adv.* **2020**, *6*, eabb9823.
(48) Zhang, X.; Shi, R.; Li, Z.; Zhao, J.; Huang, H.; Zhou, C.; Zhang, T. Photothermal-assisted photocatalytic nitrogen oxidation to nitric acid on palladium-decorated titanium oxide. *Adv. Energy Mater.* **2022**, *12*, 2103740.
(49) Wang, Y.; Denisov, N.; Qin, S.; Gonçalves, D. S.; Kim, H.; Sarma, B. B.; Schmuki, P. Stable and highly active single atom configurations for photocatalytic H_2 generation, *Adv. Mater*. **2024**, *36*, 2400626.
(50) DeRita, L.; Dai, S.; Lopez-Zepeda, K.; Pham, N.; Graham, G. W.; Pan, X.; Christopher, P. Catalyst architecture for stable single atom dispersion enables site-specific spectroscopic and reactivity measurements of CO adsorbed to Pt atoms, oxidized Pt clusters, and metallic Pt clusters on TiO_2. *J. Am. Chem. Soc.* **2017**, *139*, 14150−14165.
(51) Guo, M.; Kong, X.; Li, C.; Yang, Q. Hydrogenation of benzoic acid derivatives over Pt/TiO_2 under mild conditions. *Commun. Chem.* **2021**, *4*, 54.
(52) Qin, S.; Will, J.; Kim, H.; Denisov, N.; Carl, S.; Spiecker, E.; Schmuki, P. Single atoms in photocatalysis: low loading is good enough!. *ACS Energy Lett.* **2023**, *8*, 1209−1214.
(53) Rej, S.; Hejazi, S. M. H.; Badura, Z.; Zoppellaro, G.; Kalytchuk, S.; Kment, Š.; Fornasiero, P.; Naldoni, A. Light-induced defect formation and Pt single atoms synergistically boost photocatalytic H_2 production in 2D TiO_2-bronze nanosheets. *ACS Sustainable Chem. Eng.* **2022**, *10*, 17286−17296.
(54) Chen, W.; Zheng, W.; Cao, J.; Fu, W.; Qian, G.; Chen, D.; Zhou, X.; Duan, X. Atomic insights into robust Pt−PdO interfacial site-boosted hydrogen generation. *ACS Catal.* **2020**, *10*, 11417−11429.
(55) Li, J.; Guan, Q.; Wu, H.; Liu, W.; Lin, Y.; Sun, Z.; Ye, X.; Zheng, X.; Pan, H.; Zhu, J.; Chen, S.; Zhang, W.; Wei, S.; Lu, J. Highly active and stable metal single-atom catalysts achieved by strong electronic metal−support interactions. *J. Am. Chem. Soc.* **2019**, *141*, 14515−14519.
(56) Zhang, T.; Zhao, Z.; Zhang, D.; Liu, X.; Wang, P.; Li, Y.; Zhan, S. Superexchange-induced Pt-O-Ti^{3+} site on single photocatalyst for efficient H_2 production with organics degradation in wastewater. *Proc. Natl. Acad. Sci.* **2023**, *120*, e2302873120.
(57) Miller, J.; Meyers, B.; Barr, M.; Modica, F.; Koningsberger, D. Hydrogen temperature-programmed desorptions in platinum catalysts: Decomposition and isotopic exchange by spillover hydrogen of chemisorbed ammonia. *J. Catal.* **1996**, *159*, 41−49.
(58) Setvín, M.; Aschauer, U.; Scheiber, P.; Li, Y.-F.; Hou, W.; Schmid, M.; Selloni, A.; Diebold, U. Reaction of O_2 with subsurface oxygen vacancies on TiO_2 anatase (101). *Science*, **2013**, *34*, 988−991.
(59) Setvín, M; Schmid, M.; Diebold, U. Aggregation and electronically induced migration of oxygen

vacancies in TiO_2 anatase. *Phys. Rev. B* **2015**, *91*, 195403.
(60) Wang, Y.; Zhao, D.; Ji, H.; Liu, G.; Chen, C.; Ma, W.; Zhu, H.; Zhao, J. Sonochemical hydrogen production efficiently catalyzed by Au/TiO_2, *J. Phys. Chem. C* **2010**, *114*, 17728–17733.
(61) Xu, B.-B.; Zhou, M.; Ye, M.; Yang, L.-Y.; Wang, H.-F.; Wang, X.; Yao, Y.-F. Cooperative motion in water–methanol clusters controls the reaction rates of heterogeneous photocatalytic reactions. *J. Am. Chem. Soc.* **2021**, *143*, 10940−10947.
(62) He, Q.; Zhou, Y.; Shou, H.; Wang, X.; Zhang, P.; Xu, W.; Qiao, S.; Wu, C.; Liu, H.; Liu, D.; Chen, S.; Long, R.; Qi, Z.; Wu, X.; Song, L. Synergic reaction kinetics over adjacent ruthenium sites for superb hydrogen generation in alkaline media. *Adv. Mater.* **2022**, *34*, 2110604.